Computers & Geosciences 133 (2019) 104310

Contents lists available at ScienceDirect

Computers and Geosciences

journal homepage: www.elsevier.com/locate/cageo

Research paper

Adaptive Importance Sampling Unscented Kalman Filter based SAR image super resolution

Sithara Kanakaraj [a,1], Madhu S. Nair [b,*,1], Saidalavi Kalady [a,1]

[a] Department of Computer Science and Engineering, National Institute of Technology, Calicut 673601, Kerala, India
[b] Department of Computer Science, Cochin University of Science and Technology, Kochi 682022, Kerala, India

ARTICLE INFO

Keywords:
Super resolution
Synthetic Aperture Radar image
Importance sampling
Unscented Kalman Filter
Adaptive algorithm
Noise covariance

ABSTRACT

Enhancing Synthetic Aperture Radar (SAR) images for sharp and detailed images through super-resolution (SR) is of great significance in many remote sensing applications. Due to the inherent resolution limitations and the cost incurred for further development of sensor devices, image enhancements through image processing techniques have become more popular. However, in these techniques, the soft edges present in the images are not reconstructed completely, thereby marring the clarity of the generated image. This paper presents a method to restore more details in the image by adaptively adjusting the measurement noise covariance and process noise covariance into the intensity estimation framework for SAR image super-resolution. For this, an Adaptive Importance Sampling Unscented Kalman Filter (ISUKF) framework is implemented using the covariance matching technique. Experimental results indicate that the super-resolution using ISUKF framework performs better, regarding denoising and feature preservation, when accounted for the measurement and process noise covariance. It also outperforms the other recent and standard SR techniques covered in the literature.

1. Introduction

Resolution enhancement of images in the satellite domain, especially Synthetic Aperture Radar (SAR) images, is a very active area of research. SAR images are more popular than other radar imaging modalities due to its usability under different weather conditions and the excellent quality of cloud-free images developed. The super-resolution (SR) of SAR images overcome the inherent resolution limitations of the imaging device, thereby preparing the images for utilization in other remote sensing image applications like military systems, environmental-mapping, etc. The speckle noise present in the images from Radar image acquisition devices makes the resolution enhancement a challenging procedure. Improving the Radar/SAR sensors for higher quality images would be costly. Hence, resolution enhancement through image processing techniques like SR proves to be an inevitable alternative for such enhancements.

Works in the recent literature of image SR focuses more on exploiting the sparsity of the desired image over an over-complete dictionary (He et al., 2012; Yang et al., 2010). Another alternative is framing SR as an inverse problem for recovering the high-resolution frame from several low-resolution frames providing more details of the desired reconstructed output. This method is still attempted, even though the output quality is highly dependent on the image registration accuracy of the low-resolution frames. In learning based SR techniques (Freeman et al., 2002; Dong et al., 2016), the reconstruction accuracy confronts a trade-off between the computational cost and the size of the training data. Authors have also attempted image SR techniques using the estimation theory. They have worked with prior assumptions on the linear Kalman Filter parameters (Newland et al., 2006; Newland and Gray, 2005; Wei et al., 2014) to reduce the computational load. But, these assumptions suppress the output quality of the image. SR methodologies proposed in the literature for natural images, with linear noise (additive noise), fail when used on the SAR image dataset. The cause for this failure is the inherent speckle noise in SAR images. However, variants of Kalman Filter (KF) that accounts for the non-linear systems like Extended KF (Rosales and Sclaroff, 1999) and Unscented KF (UKF) (Sarkka, 2007) have also been developed in other domains.

The UKF estimation procedure applied to other domains like Battery State-of-Charge (SoC) estimation, Target Tracking, etc., are also gaining popularity. Variations to the conventional UKF to adapt to the dynamic changes in the environment have been widely proposed in these domains. The fixed filter design does not account for the process noise covariance (Q) or the measurement noise covariance (V). The

* Corresponding author.
E-mail addresses: sitharavp@gmail.com (S. Kanakaraj), madhu_s_nair2001@yahoo.com (M.S. Nair), said@nitc.ac.in (S. Kalady).
[1] All the authors have equally contributed in the formulation of the algorithm and the experimental analysis.

https://doi.org/10.1016/j.cageo.2019.104310
Received 26 June 2018; Received in revised form 29 April 2019; Accepted 3 August 2019
Available online 5 August 2019
0098-3004/

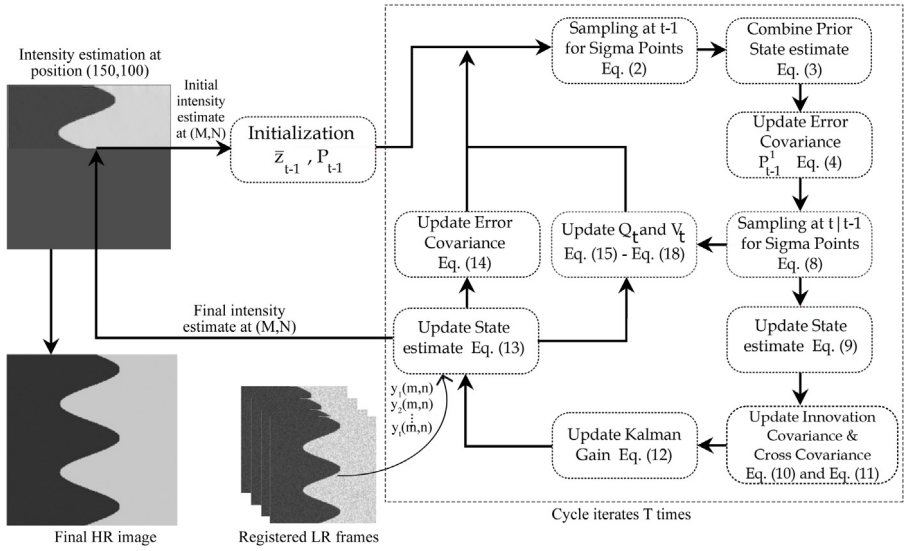

Fig. 1. Overview of the proposed system.

Adaptive UKF framework proposed in the literature acknowledges a wide range of environmental conditions. The conventional UKF framework assumes prior knowledge of the Q and V statistics. If we choose a smaller initial value for V/Q, the uncertainty around true value is lesser (Almagbile et al., 2010). And if we choose a large initial value, the filter diverges. Thus, the fixed estimation framework must be replaced to accommodate the dynamics in the environment adaptively.

To account for Q and V, most of the research in the literature preferred the covariance matching technique to achieve more accurate estimation. Adaptive UKF has been widely proposed for SoC estimation in batteries with different battery models (Sun et al., 2011; Zhang et al., 2015; Partovibakhsh and Liu, 2014). Meng et al. (2016) proposed an Adaptive UKF combined with Support Vector Machine that requires very few initial samples for accurate estimation. The technique uses a moving window mechanism to achieve accuracy from limited samples. Zhou et al. (2017) proposed a technique to detect filter divergence in case of non-linear systems involving model mismatches using the covariance matching. In addition to this, an adaptive weighted coefficient was also developed to restrict the divergence. Recent work by Liu et al. (2017) has also proposed an adaptive square root UKF to estimate the SoC estimate in batteries.

Application of the Importance Sampling UKF (ISUKF) (Jojy et al., 2013) has been successfully demonstrated in Kanakaraj et al. (2018) for SAR image super-resolution. In order to improve the quality of the desired HR image, we have modified the ISUKF framework to adapt to the measurement noise covariance and process noise covariance using the covariance matching technique. In this work, we have considered the measurement covariance error to be more critical. This has been done so, as the LR images are assumed to be taken in a time series and also because each frame would have different noise statistics.

The remainder of the paper is organized as follows. A brief description of basic ISUKF framework for SAR image super-resolution is given in Section 2. The adaptive ISUKF framework has been described in Section 3. Section 4 discusses the results and outcomes based on the comparison of the proposed work with the recent state-of-the-art techniques for SAR image super-resolution. Finally, Section 5 concludes the work.

2. Background

Super-resolution aims to enhance the resolution of the LR images to a sharper and more detailed high resolution image. The input models considered in the image SR literature assumes the LR images to be degraded with white Gaussian noise alone, while SAR images are inherently degraded with the presence of granular/ multiplicative noise. Improving the resolution of SAR images using the general image SR techniques can fail due to the inherent speckle noise in SAR image. Thus the SR technique developed to deal with SAR images needs to tackle the speckle noise present in it. In our previous work (Kanakaraj et al., 2018), we had designed an ISUKF based framework that enhances the resolution of SAR images, in particular, and deals with the speckle noise simultaneously.

In this section we provide an overview of the existing ISUKF system. The Importance Sampling Unscented Kalman Filter is a recursive UKF framework with a Discontinuity-Adaptive Markov Random Field (DAMRF) prior, to account for the speckle noise in the system (Jojy et al., 2013). Here, Importance Sampling is used to predict the first two moments (mean and variance) of the conditional PDF. The values forecasted are then propagated through the multiplicative image model under consideration to estimate the original pixel intensity.

A brief outline of the steps involved in ISUKF for SAR image super-resolution (Kanakaraj et al., 2018) is as follows:

1. **LR registration:** We begin with an image registration procedure to align the input LR images, that are degraded with translational motion and speckle noise. The LR images are registered to a common base image, i.e., one of the LR images, using a subpixel registration algorithm (Guizar-Sicairos et al., 2008). The pixel intensity at position (m,n) of each LR image y_t is considered as the measurement value at time $t, t = 1..T$.
2. **Noise Estimation and Initialization:** Next, we estimate the noise variance in the LR images. Due to the random fluctuations of the echoed radar signals, the noise levels in the SAR image are unknown. Hence, a noise level estimator (Liu et al., 2013) is used to determine the noise variance in the LR images. The output HR frame is initialized with the mean of the first five rows of the base LR image.
3. **Combined super-resolution and speckle removal:** The registered LR images along with the estimated noise level are given as input to the framework. T cycles of the ISUKF estimates a single pixel intensity of the HR frame from the T LR frames. The relation between a pixel position (m,n) in the LR frame upsampled by a factor d to a pixel position (M,N) in HR frame is defined as, $M \in \{d \times m - i\}$ and $N \in \{d \times n - j\}; 0 \le i,j \le d-1$. The initial HR value at pixel position (M,N) is considered as the initial estimate. With the intensity values at position (m,n) of each LR image being the measurement value input for each

iteration in an ISUKF cycle, the recursive UKF converges to the estimated value.

In the ISUKF procedure, we have excluded the process noise covariance and measurement noise covariance in the prediction and updation steps, respectively. The above framework has been further elaborated in Kanakaraj et al. (2018).

The Adaptive ISUKF proposed in this paper has been modified to include both the noise covariance statistics in order to adaptively accommodate the dynamics in the environment thereby improving the reconstructed quality of the output image. The next section elaborates on the proposed methodology.

3. Proposed methodology

As mentioned in the previous section, the ISUKF assumed the measurement noise covariance and process noise covariance to be zero. However, the proposed adaptive ISUKF is modified to adaptively adjust to the noise variance dynamics in the environment. Fig. 1 depicts a schematic diagram of the adaptive ISUKF (AISUKF) technique proposed in this paper. The estimation procedure for a single pixel intensity at position (M, N) of the HR image depicted in the figure is repeated to reconstruct each pixel in the final HR image. The initial estimate is a constant value at position (M, N) of the HR frame. The initialized intensity estimate and covariance matrix are fed as input into the AISUKF procedure. Eqs. (2)–(14) are iterated T times, with each iteration taking one measurement value at location (m, n) from the T registered LR images. After T iterations, the final intensity value at position (M, N) is estimated and interchanged with the initial estimate. The highlighted boxes in the diagram show changes proposed in order to accommodate the noise variance statistics into the ISUKF procedure proposed in Kanakaraj et al. (2018). The proposed framework is briefed below:

1. Model Representation and Initialization
   In the case of synthetic images, the input LR images, y_t, used to form the enhanced HR image can be represented as follows:

$$y_t = dF_tX * v_t, \qquad t = 1, \ldots, T \tag{1}$$

   where d is the decimation factor of the original image X, F is the global shift applied to the image to generate multiple LR frames and v_t is the variance of the speckle noise. In the case of real SAR images, the acquired SAR image is considered as the degraded input y_t.
   An autoregressive model is used for the reconstruction of the HR frame. The results of the previous state act as the input to predict the output of the next state. To estimate a pixel (M, N) in the HR frame, the Adaptive ISUKF procedure is iteratively run for T times with the intensity at position (m, n) in $y_t, t = 1, \ldots, T$ as the measurement value. The initialization of the intensity estimate, $\bar{z}_{t-1}$, and Covariance Matrix, P_{t-1}, is calculated similar to that in Kanakaraj et al. (2018). The measurement noise covariance V_0 is initialized to 0.5, process noise covariance Q_0 is initialized to 0.01 and the window size for covariance matching, L, is initialized to 15 (Sun et al., 2011).
2. Prediction Step
   (a) Compute Sigma points and their weights at Step $t-1$

$$S_{t-1} = \left[\bar{z} \quad \bar{z} \pm \sqrt{(n_a + \lambda)P}\right] \tag{2}$$

   where n_a is the dimension of $\bar{z}$, λ is the scaling parameter and S_{t-1} is the augmented sigma point matrix with dimension $n_a \times (2n_a + 1)$ at time step $t-1$.

   (b) Combine Prior intensity estimate and update error covariance at Step $t-1$

$$z^1_{t|t-1} = \sum_{i=0}^{2n_a} w^i_\mu S^i_{t-1} \tag{3}$$

$$P^1_{t|t-1} = \sum_{i=0}^{2n_a} w^i_c (S^i_{t-1} - z^1_{t|t-1})(S^i_{t-1} - z^1_{t|t-1})^T + Q_{t-1} \tag{4}$$

   where $z^1_{t|t-1}$ is the prediction from sigma points at time step $t-1$, and w^i_μ and w^i_c are the mean and covariance weights, respectively.

$$w^0_\mu = \frac{\lambda}{(n_a + \lambda)} \tag{5}$$

$$w^0_c = w^0_\mu + (1 - \alpha^2 + \beta) \tag{6}$$

$$w^i_c = w^i_\mu = \frac{1}{2(n_a + \lambda)}, \qquad \text{for } 1 \le i \le 2n_a \tag{7}$$

   Here, α is the spread of sigma points and, $\beta = 2$ (in the case of Gaussian distribution) (Kanakaraj et al., 2018) is used to incorporate prior knowledge.

3. Updation Step
   (a) Compute Sigma points and their weights at Step $t|t-1$

$$S_{t|t-1} = \left[z^1_{t|t-1} \quad z^1_{t|t-1} \pm \sqrt{(n_a + \lambda)P^1_{t|t-1}}\right] \tag{8}$$

   where $S_{t|t-1}$ are the sigma points at time step $t|t-1$.
   (b) Update the intensity estimate, innovation covariance and cross covariance from the transformed sigma points

$$z^2_{t|t-1} = \sum_{i=0}^{2n_a} w^i_\mu S^i_{t|t-1} \tag{9}$$

$$P_{IC_t} = \sum_{i=0}^{2n_a} w^i_c (S^i_{t|t-1} - z^2_{t|t-1})(S^i_{t|t-1} - z^2_{t|t-1})^T + V_{t-1} \tag{10}$$

$$P_{CC_t} = \sum_{i=0}^{2n_a} w^i_c (S^i_{t-1} - z^1_{t|t-1})(S^i_{t|t-1} - z^2_{t|t-1})^T \tag{11}$$

   where $z^2_{t|t-1}$ is the predicted intensity value for the sigma points at time step $t|t-1$, P_{IC_t} is the innovation covariance of the predicted intensity values at time step $t|t-1$, and P_{CC_t} is the cross covariance between predictions of intensity value at time step $t-1$ and $t|t-1$.
   (c) Compute Kalman Gain

$$K = P_{CC} * (P_{IC})^{-1} \tag{12}$$

   (d) Compute the intensity estimate and error covariance at time step t

$$\bar{z}_t = z^1_{t|t-1} + K(x_t - z^2_{t|t-1}) \tag{13}$$

   where x_t is the intensity at position (m, n) of LR image y_t.

$$P_t = P_{t|t-1} - K * P_{IC} * K^T \tag{14}$$

4. Calculate V_t and Q_t

$$E_t = x_t - (\bar{z} * v) \tag{15}$$

   where v is the estimated noise variance.

$$F_t = \frac{1}{L} * \sum_{n=t-L+1}^{t} E_t E_t^T \tag{16}$$

$$V_t = F_t + \sum_{i=0}^{2n_a} w^i_{(c)} (S^i_{t|t-1} - x_t + E_t)(S^i_{t|t-1} - x_t + E_t)^T \tag{17}$$

$$Q_t = K * F_t * K' \tag{18}$$

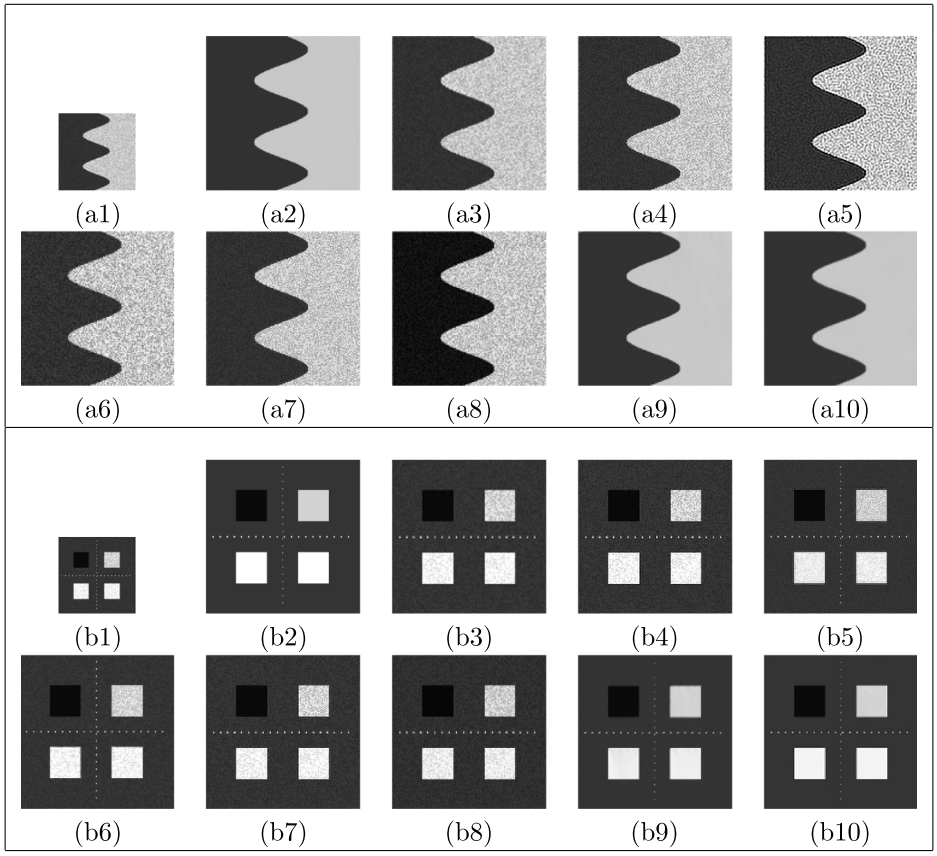

Fig. 2. Experimental results on (a) Synthetic Image and (b) Phantom Image. (a1, b1) LR image with a noise variance of 0.01 (128 × 128), (a2, b2) Original image (256 × 256), (a3, b3) Bicubic Interpolation (256 × 256), (a4, b4) SR via Sparse Representation (Yang et al., 2010) (256 × 256), (a5, b5) Combined Debluring and SR method (Dong et al., 2011) (256 × 256), (a6, b6) SR using Kalman Filter (Wei et al., 2014) (256 × 256), (a7, b7) SR using Deep networks with sparse Prior (Wang et al., 2015) (256 × 256), (a8, b8) Multistage iterative SR (Shkvarko et al., 2016) (256 × 256), (a9, b9) SR using ISUKF (Kanakaraj et al., 2018) (256 × 256), and (a10, b10) Proposed Adaptive ISUKF method (256 × 256).

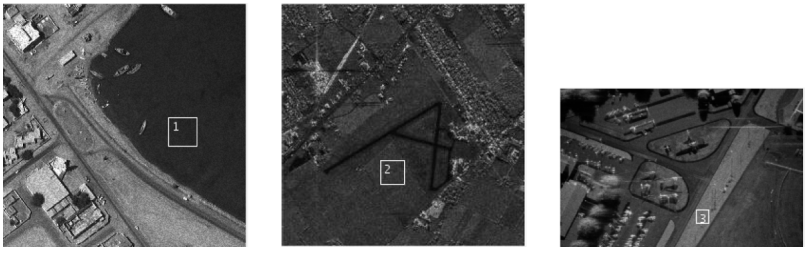

Fig. 3. Original SAR images. (a) Island image (256 × 256) (b) SAR Image 1 (256 × 256), and (c) SAR Image 2 (256 × 166).

The covariance matching technique is used to accommodate the process and measurement noise covariance statistics. We compute the intensity residual E_t along with V_t and Q_t at time step t to be used for the next prediction and update process at step $t+1$.

The above steps are iteratively performed for T times representing the T LR images, with the intensity at position (m,n) taken as the measurement value for each iteration. The Adaptive ISUKF procedure is repeated for the size of HR image. This is followed by Discontinuity Adaptive Non Local Mean (DA-NLM) filtering (Jojy et al., 2013) as a post-processing step.

4. Results and discussion

We have compared the proposed Adaptive ISUKF method with ISUKF and other standard works from the recent past, wherein the above-stated method has superior results with better denoising and feature preservation qualities. The quantitative metrics in the tables and visual inspection of the figures indicate the out-performance of the proposed technique. The clarity and detail preservation is evidently seen in the enlarged portions of the SR images.

Performance comparison of the proposed method with the earlier standard methods was assessed using qualitative and quantitative metrics. The works considered for comparison include resolution enhancement using sparse representation (Yang et al., 2010), using deblurring and SR together (Dong et al., 2011), using Kalman Filter (Wei et al., 2014), using deep networks (Wang et al., 2015), using an iterative multistage approach (Shkvarko et al., 2016), using the ISUKF (Kanakaraj et al., 2018) and also using the traditional bicubic interpolation. Both full reference metrics (PSNR, SSIM, FSIM, EPF) and non-reference metric (ENL) are used to evaluate the reconstruction method on two test images (Fig. 2(a2), 2(b2)) and three SAR images (Fig. 3(a), 3(b), 3(c)), respectively.

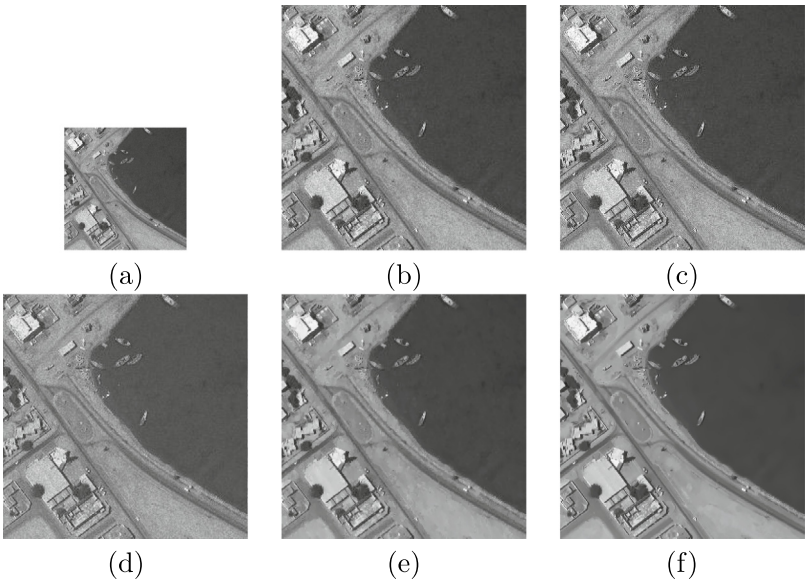

Fig. 4. Experimental results on SAR image 1. (a) Original SAR image (256×256), (b) SR using Kalman Filter (Wei et al., 2014) (512×512), (c) SR using Deep networks with sparse Prior (Wang et al., 2015) (512 × 512), (d) Multistage iterative SR (Shkvarko et al., 2016) (512 × 512), (e) SR using ISUKF (Kanakaraj et al., 2018) (512 × 512), and (f) Proposed AISUKF method (512 × 512).

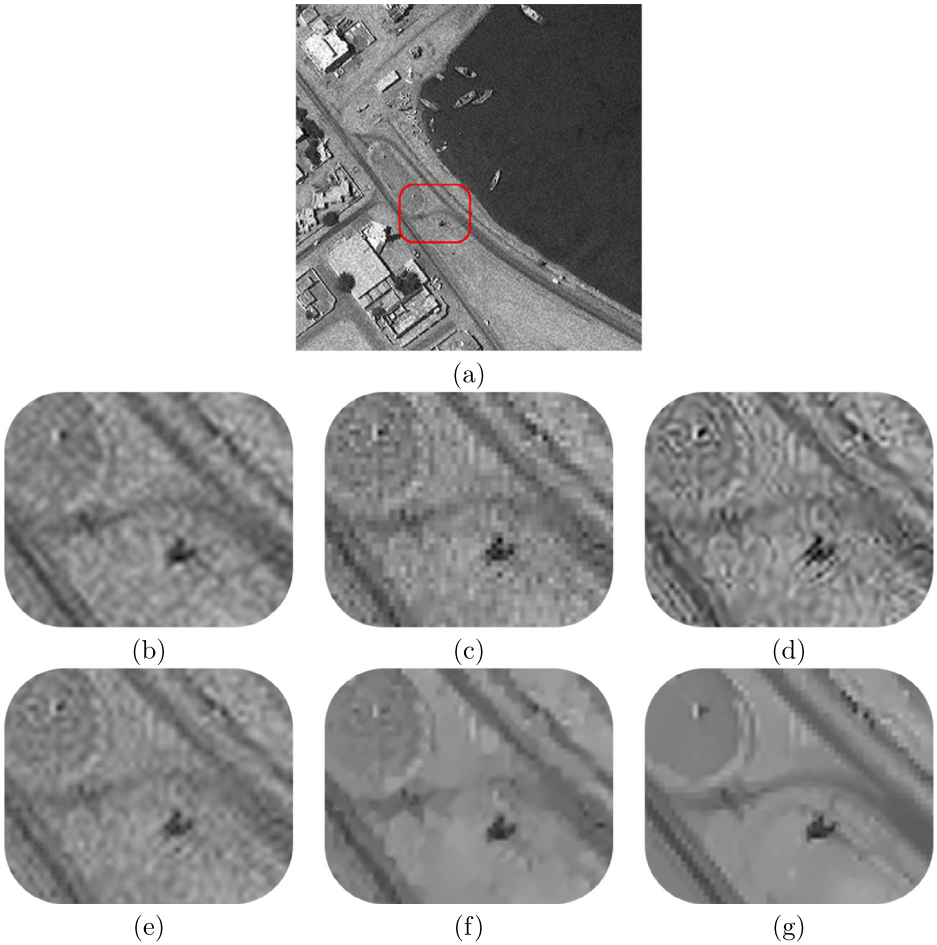

Fig. 5. Focused region of the SR result on SAR Image 1. (a) Original SAR image marked with the focused region, (b) Original Image, (c) SR using Kalman Filter (Wei et al., 2014), (d) SR using Deep networks with sparse Prior (Wang et al., 2015), (e) Multistage iterative SR (Shkvarko et al., 2016), (f) SR using ISUKF (Kanakaraj et al., 2018), and (g) Proposed AISUKF method.

The synthetic test images in Fig. 2(a2) and Fig. 2(b2), is degraded and combined with a fully developed exponential speckle of variance 0.01 as noise to produce multiple LR images (Fig. 2(a1) and Fig. 2(b1)). This design is adopted to imitate the real SAR image scenario. Whereas,

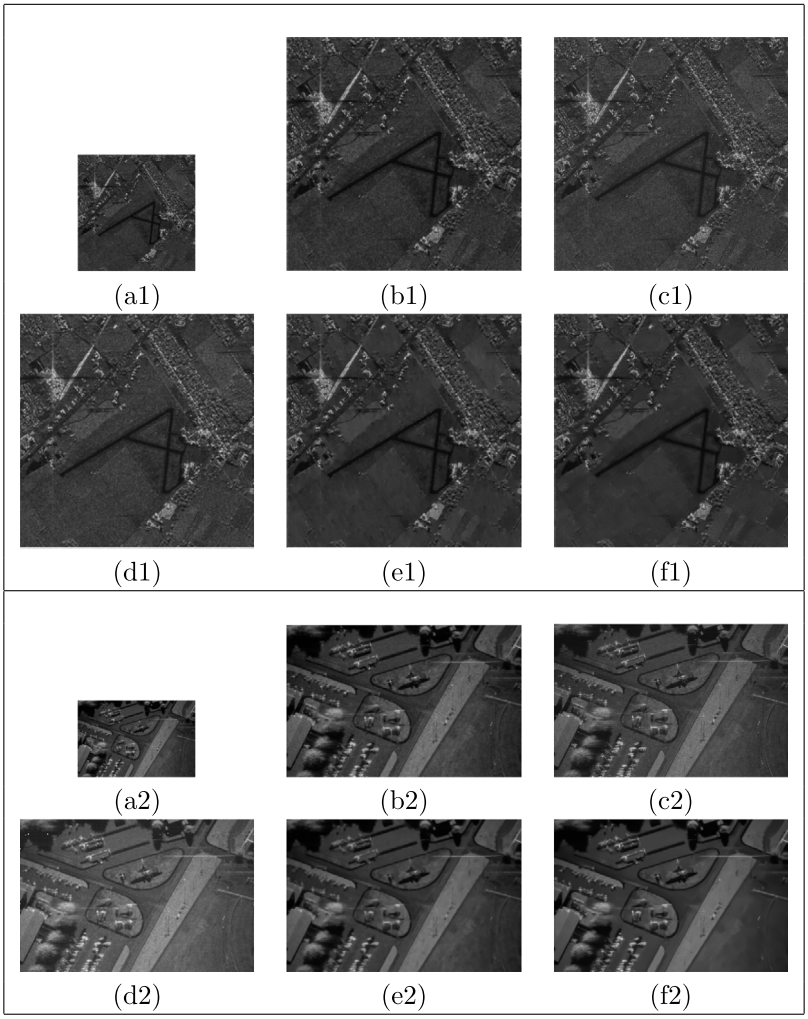

Fig. 6. Experimental results on SAR images. (a1, a2) Original SAR image, (b1, b2) SR using Kalman Filter (Wei et al., 2014), (c1, c2) SR using Deep networks with sparse Prior (Wang et al., 2015), (d1, d2) Multistage iterative SR (Shkvarko et al., 2016), (e1, e2) SR using ISUKF (Kanakaraj et al., 2018), and (f1, f2) Proposed AISUKF method.

the real SAR images are taken as input directly from the acquisition device without further degradation. The framework uses the degraded LR image as the input and produces a reconstructed image with higher resolution as the output. We have chosen a magnification factor of 2 for experimentation. The SAR images used for evaluation in Fig. 3(a) are taken from Masirah Island Oman (Satellite Imaging Corporation, 2018), Fig. 3(b) Airport image taken from NASA/JPL (Kanakaraj et al., 2018), and Fig. 3(c) taken from Sandia Lab Airborne Tests (Synthetic Aperture Radar, 2018).

For the synthetic image and phantom image, the reconstruction quality of the output images are compared quantitatively in Tables 1 and 2. Whereas, we have evaluated the SAR images by measuring the noise suppression in a homogeneous region in the resolution enhanced real SAR images. The ENL values in Table 3 also depict the same. With a visual inspection of Figs. 4 and 6, representing the super-resolved SAR images, and Fig. 5 depicting an enlarged portion from one of the SAR image, the quality of feature preservation can be noted. The following are the assessment metrics used for evaluation.

1. Peak signal-to-noise ratio (**PSNR**)$= 10 * log\left[\frac{255^2}{\frac{1}{M*N}\sum_{i=1}^{M}\sum_{j=1}^{N} d^2(i,j)}\right]$
   where d indicates the change between the original image and the reconstructed image of size $M \times N$ (He et al., 2012). A higher index indicates lower noise level in the image.
2. Structural Similarity Index Measure (**SSIM**) $= L(x,y) * C(x,y) * S(x,y)$
   where L, C and S are the change in luminance, contrast and structure, respectively (Jojy et al., 2013). Index closer to 1 indicates more similarity.
3. Feature Similarity Index Measure (**FSIM**) $= \frac{\sum_x S(x).PC_m(x)}{\sum_x PC_m(x)}$
   where $S(x)$ is the local similarity at location x and $PC_m(x)$ is the maximum phase congruency value between f_1 and f_2 at location x (Zhang et al., 2011). Index closer to 1 indicates more similarity.
4. Edge Preservation Factor (**EPF**) $= \frac{\sum(\Delta x-\overline{\Delta x})(\Delta y-\overline{\Delta y})}{\sqrt{\sum(\Delta x-\overline{\Delta x})^2\sum(\Delta y-\overline{\Delta y})^2}}$
   where Δx and Δy are the edge filtered images of x and y, respectively and $\overline{\Delta x}$ and $\overline{\Delta y}$ are their mean values (Sattar et al., 1997). A value closer to 1 indicates optimal edge preservation.
5. Equivalent Number of Looks (**ENL**) $= ENL = \left(\frac{\mu_f}{\sigma_f}\right)^2$
   where μ_f is the mean and σ_f is the standard deviation of a homogeneous region f (Li et al., 1983). Higher value indicates smoother region, i.e., reduced presence of speckle.

Fig. 2(a1, b1) represents a single frame from the multiple LR input images, Fig. 2(a3–a9, b3–b9) shows the resulting HR images from other methods in the literature and Fig. 2(a10, b10) shows the resolution enhanced result of the proposed Adaptive ISUKF super-resolution technique. A visual analysis of the HR images of Fig. 2 reveals the superiority of the proposed method over other techniques. In Fig. 2(a10), the curved edges are sharper, and the homogeneous regions are smoother when compared to Fig. 2(a9). It can be observed that the vertical and

Table 1
Performance evaluation results of SR techniques on synthetic image.

	PSNR	SSIM	FSIM	EPF
Bicubic interpolation	25.7809	0.5544	0.8925	0.6760
Yang et al. (2010)	22.0952	0.3847	0.8842	0.4539
Dong et al. (2011)	18.2676	0.3349	0.8900	0.4809
Wei et al. (2014)	20.4948	0.2013	0.3531	0.3002
Wang et al. (2015)	21.9307	0.3810	0.8842	0.3972
Shkvarko et al. (2016)	18.5528	0.2858	0.8389	0.3894
Kanakaraj et al. (2018)	31.6144	0.9797	0.9932	0.7455
Proposed	**32.6717**	**0.9841**	**0.9943**	**0.7931**

Table 2
Performance evaluation results of SR techniques on phantom image.

	PSNR	SSIM	FSIM	EPF
Bicubic interpolation	24.7961	0.7144	0.8921	0.2892
Yang et al. (2010)	22.8084	0.5628	0.5105	0.1515
Dong et al. (2011)	25.0854	0.1953	0.5499	**0.6455**
Wei et al. (2014)	23.9066	0.1645	0.6537	0.1586
Wang et al. (2015)	22.9884	0.5624	0.8793	0.2234
Shkvarko et al. (2016)	23.1042	0.1427	0.6078	0.1130
Kanakaraj et al. (2018)	27.8791	0.9455	0.9609	0.5034
Proposed	**28.5355**	**0.9554**	**0.9955**	0.5124

horizontal dotted lines in the phantom image are affected at large by the super-resolution process. In Fig. 2(b3, b4, b7, b8) the vertical dotted lines are missing. In Fig. 2(b5,b6) the dotted lines are visible, but the presence of noise degrades the quality of the output. Even though Fig. 2(a9) is structurally similar to the original image and noise free; Fig. 2(b10) is sharper than Fig. 2(b9). The values of the assessment metrics in Tables 1 and 2 also supports the superiority of the proposed work. From Table 1, the metric values of the proposed technique show an increase of 1.06 dB in PSNR, 0.004 increase in SSIM value, and 0.05 increase in EPF value. And, from Table 2, there is an increase of 0.7dB in PSNR, 0.04 increase in FSIM value, and 0.01 increase in EPF value indicating denoising and sharper edges, respectively.

Evaluation of the super-resolved SAR images cannot be done using the full-reference assessment metrics discussed earlier, due to the absence of the desired HR output. Therefore, we have only measured the noise reduction in a homogenous region and pictorially focused on the areas of the image that shows detail preservation. SAR image 2 is super resolved to the size (512×512) and SAR image 3 is super resolved to size (512×332). The super-resolution results of some of the recent works have been added in Figs. 4 and 6. We have selected one homogeneous region from each SAR image in Fig. 3 to calculate the ENL values in Table 3. Region 1, Region 2 and Region 3, corresponds to one region from Fig. 3(a), Fig. 3(b) and Fig. 3(c), respectively. From the ENL values in Table 3, we can observe an increase of more than 200 in our proposed method. Higher ENL value indicates a smoother homogenous region, i.e., better noise suppression.

From the tables and figures, the significant improvement of the proposed technique by adapting the covariances values can be noted. The quality of feature preservation of the proposed method can be examined from the zoomed portion of the super-resolved SAR image in Fig. 5. The zoomed portion of the SAR image is marked in Fig. 5(a). It shall be observed that the mud roads in the images are clearer and sharper in the proposed technique (Fig. 5(g)). The SR results of the proposed method and other compared methods on SAR image 2 and SAR image 3 are shown in Fig. 6(b1–f1) (512 × 512) and Fig. 6(b2–f2) (512 × 332), respectively. Together with the quantitative analysis and visual analysis, the estimation accuracy of the proposed Adaptive ISUKF super-resolution technique is more evident.

4.1. Computer code availability

The code associated with this paper is available in the Github repository https://github.com/sitharavpk/Adaptive-ISUKF . All the implementations were performed in MATLAB on a Windows 7 machine with an Intel Core i5 processor, 8-GB RAM, and 64-bit OS. The repository contains the test images, both synthetic and real SAR images, along with the publicly available codes for image registration, noise level estimation from a single image and the quality assessment metrics like SSIM and FSIM.

Table 3
ENL measure of homogeneous regions in real SAR images.

	Region 1	Region 2	Region 3
Input noisy LR image	202.2504	51.6516	218.8580
Yang et al. (2010)	177.0252	34.7740	152.1160
Dong et al. (2011)	119.4345	18.6002	8.3742
Wei et al. (2014)	201.6900	51.7849	224.2241
Wang et al. (2015)	191.4637	66.3455	218.6429
Shkvarko et al. (2016)	83.1964	54.8246	333.8916
Kanakaraj et al. (2018)	582.8840	248.1248	826.7959
Proposed	**1038.1**	**468.6289**	**1099.4000**

5. Conclusion

In this paper, we have proposed an Adaptive ISUKF for better super-resolution of SAR images. The proposed technique is applicable on time-series SAR images. Due to the unavailability of real public dataset of time-series SAR images, the method has been tested on synthetic time-series images generated by considering the actual acquisition scenario of time-series SAR images. Earlier, the ISUKF framework for SAR image super-resolution had a fixed filter design that neither accounted for the process noise covariance (Q) nor the measurement noise covariance (V). A modification to the existing algorithm to adaptively accommodate the dynamics in the environment is attempted in this work. The covariance matching technique is used to adjust the noise covariances adaptively. The analysis of the super-resolution results, indicates the superior performance of the proposed method, both visually and analytically. The results have been proven to be promising and thus, it can be assured that the technique would give good results in real time-series SAR images as well.

The denoising and feature preservation qualities are evident from the SAR image super-resolution results. A comparison of the proposed work with the existing techniques in the domain also shows significantly higher values for the quantitative assessment metrics. The proposed technique also demonstrates its ability to capture the soft edges in the SAR images. Therefore, accommodating the covariance values has proved to be highly beneficial for more accurate intensity estimation.

References

Almagbile, A., Wang, J., Ding, W., 2010. Evaluating the performances of adaptive Kalman filter methods in GPS/INS integration. J. Glob. Position. Syst. 9 (1), 33–40.
Dong, C., Loy, C.C., He, K., Tang, X., 2016. Image super-resolution using deep convolutional networks. IEEE Trans. Pattern Anal. Mach. Intell. 38 (2), 295–307.
Dong, W., Zhang, L., Shi, G., Wu, X., 2011. Image deblurring and super-resolution by adaptive sparse domain selection and adaptive regularization. IEEE Trans. Image Process. 20 (7), 1838–1857.
Freeman, W.T., Jones, T.R., Pasztor, E.C., 2002. Example-based super-resolution. IEEE Comput. Graph. Appl. 22 (2), 56–65.
Guizar-Sicairos, M., Thurman, S.T., Fienup, J.R., 2008. Efficient subpixel image registration algorithms. Opt. Lett. 33 (2), 156–158.
He, C., Liu, L., Xu, L., Liu, M., Liao, M., 2012. Learning based compressed sensing for SAR image super-resolution. IEEE J. Sel. Top. Appl. Earth Obs. Remote Sens. 5 (4), 1272–1281.
Jojy, C., Nair, M.S., Subrahmanyam, G., Riji, R., 2013. Discontinuity adaptive non-local means with importance sampling unscented Kalman filter for de-speckling SAR images. IEEE J. Sel. Top. Appl. Earth Obs. Remote Sens. 6 (4), 1964–1970.

Kanakaraj, S., Nair, M.S., Kalady, S., 2018. SAR image super resolution using importance sampling unscented Kalman filter. IEEE J. Sel. Top. Appl. Earth Obs. Remote Sens. 11 (2), 562–571.

Li, F.-K., Croft, C., Held, D.N., 1983. Comparison of several techniques to obtain multiple-look SAR imagery. IEEE Trans. Geosci. Remote Sensing (3), 370–375.

Liu, S., Cui, N., Zhang, C., 2017. An adaptive square root unscented Kalman filter approach for state of charge estimation of lithium-ion batteries. Energies 10 (9), 1345–1358.

Liu, X., Tanaka, M., Okutomi, M., 2013. Single-image noise level estimation for blind denoising. IEEE Trans. Image Process. 22 (12), 5226–5237.

Meng, J., Luo, G., Gao, F., 2016. Lithium polymer battery state-of-charge estimation based on adaptive unscented Kalman filter and support vector machine. IEEE Trans. Power Electron. 31 (3), 2226–2238.

Newland, C., Gray, D., 2005. Time invariant steady-state Kalman filter for image super-resolution. In: Image and Vision Computing New Zealand, vol. 2006. pp. 381–387.

Newland, C., Gray, D., Gibbins, D., 2006. Modified Kalman filtering for image super-resolution. In: Image and Vision Computing New Zealand, vol. 2006. pp. 79–84.

Partovibakhsh, M., Liu, G., 2014. Adaptive unscented Kalman filter-based online slip ratio control of wheeled-mobile robot. In: Intelligent Control and Automation (WCICA), 2014 11th World Congress on. IEEE, pp. 6161–6166.

Rosales, R., Sclaroff, S., 1999. 3D Trajectory recovery for tracking multiple objects and trajectory guided recognition of actions. In: Computer Vision and Pattern Recognition, 1999. IEEE Computer Society Conference on, vol. 2. IEEE, pp. 117–123.

Sarkka, S., 2007. On unscented Kalman filtering for state estimation of continuous-time nonlinear systems. IEEE Trans. Automat. Control 52 (9), 1631–1641.

Satellite Imaging Corporation, 2018. http://www.satimagingcorp.com/gallery/worldview-2/worldview-2-oman-masirah-island/, (Accessed 10 March 2018).

Sattar, F., Floreby, L., Salomonsson, G., Lovstrom, B., 1997. Image enhancement based on a nonlinear multiscale method. IEEE Trans. Image Process. 6 (6), 888–895.

Shkvarko, Y.V., Yañez, J.I., Amao, J.A., del Campo, G.D.M., 2016. Radar/SAR image resolution enhancement via unifying descriptive experiment design regularization and wavelet-domain processing. IEEE Geosci. Remote Sens. Lett. 13 (2), 152–156.

Sun, F., Hu, X., Zou, Y., Li, S., 2011. Adaptive unscented Kalman filtering for state of charge estimation of a lithium-ion battery for electric vehicles. Energy 36 (5), 3531–3540.

Synthetic Aperture Radar, 2018. http://syntheticaperturerader.com/very-high-resolution-sar-images/, (Accessed 10 April 2018).

Wang, Z., Liu, D., Yang, J., Han, W., Huang, T., 2015. Deep networks for image super-resolution with sparse prior. In: Proceedings of the IEEE International Conference on Computer Vision, pp. 370–378.

Wei, Z., Tao, F., Jun, W., 2014. Kalman filter–based method for image superresolution using a sequence of low-resolution images. J. Electron. Imaging 23 (1), 013008(1)–013008(12).

Yang, J., Wright, J., Huang, T.S., Ma, Y., 2010. Image super-resolution via sparse representation. IEEE Trans. Image Process. 19 (11), 2861–2873.

Zhang, W., Shi, W., Ma, Z., 2015. Adaptive unscented Kalman filter based state of energy and power capability estimation approach for lithium-ion battery. J. Power Sources 289, 50–62.

Zhang, L., Zhang, L., Mou, X., Zhang, D., 2011. FSIM: A feature similarity index for image quality assessment. IEEE Trans. Image Process. 20 (8), 2378–2386.

Zhou, H., Huang, H., Zhao, H., Zhao, X., Yin, X., 2017. Adaptive unscented Kalman filter for target tracking in the presence of nonlinear systems involving model mismatches. Remote Sens. 9 (7), 657–676.